Eur. Phys. J. B (2021) 94:185
https://doi.org/10.1140/epjb/s10051-021-00188-7

THE EUROPEAN PHYSICAL JOURNAL B

Regular Article - Solid State and Materials

Enhancement of optoelectronic properties of layered $MgIn_2Se_4$ compound under uniaxial strain, an ab initio study

Benali Rerbal[1,a] and Tarik Ouahrani[2,b]

[1] Laboratory of Materials Discovery, Unit of Research Materials and Renewable Energies, LEPM-URMER, University of Tlemcen, Tlemcen, Algeria
[2] Laboratoire de Physique Théorique, Université de Tlemcen, 13000 Tlemcen, Algeria

Received 11 May 2021 / Accepted 19 August 2021 / Published online 22 September 2021

Abstract. We argue that tuning the structure of a semiconductor offers abundant scope for use in a number of applications. In this work, by means of comprehensive density functional theory computations, we demonstrated that layered $MgIn_2Se_4$ could be a promising candidate for future electronic and optoelectronic technologies. To do this task, we have applied a uniaxial strain in the z-direction. The results show that $MgIn_2Se_4$ can support only a -2.5% of deformation without losing its dynamical stability. However, we showed that the effect of strain strongly affects the bonding pattern, which tends to increase the bandgap value. Both the charge density and noncovalent interactions were analyzed to understand this behavior. In addition, we saw that the application of non-hydrostatic pressure also enhanced the photocatalytic/optoelectronic performance of the investigated material, offering useful insights into layered $MgIn_2Se_4$ for future development in this area.

1 Introduction

Many lessons can be learned from the current COVID-19 pandemic, which brutally hit health, the economy, and even industry worldwide. On the one hand, disinfection with the actual procedures based on ozonation, UV irradiation, chlorination, or antibacterial agents becomes backbreaking because they cause aftereffects on the environment [1–3]. On the other hand, the energy consumption based on fossil fuels used in such procedures is a big problem for many poor countries. A transformation of the alternative energy industry is now becoming urgent. Such a new industry is rather driven towards manufacturing low-cost modules. Photocatalytic disinfection [4] techniques or even photoconversion [5] of energy can both use semiconductors to achieve their tasks. Among the present semiconductors for practical disinfection, applications are those sensitive to visible-light photons. Ternary compounds like Mg_2TiO_4 constitute an example used for photocatalytic antibacterial activity [6]. In addition, for photocatalytic CO_2 reduction, we can cite the $NiCo_2S_4$ compound [5]. Many other ternary compounds having the AM_2X_4 stoichiometry possess the advantages of high electrical conductivity, low electronegativity, rich redox properties, and suitable band structures which make them advantageous for the photocatalytic degradation process. In this manner, they can directly and effectively utilize solar energy to obtain lots of valuable chemical fuels (for example, hydrocarbons or hydrogen). An example can be found in the studies based on $ZnCo_2O_4$ [7], $NiCo_2O_4$ [8,9], $CuCo_2O_4$ [10], and $MnCo_2O_4$ [11].

Recently, much interest has been devoted to layered compounds; this type of material encompasses many other properties than its bulk counterparts because the majority of bulk materials are limited in their technological applications due to the higher rate of photogenerated carriers and the electron–hole recombination process. Zinc indium sulfide ($ZnIn_2S_4$) [12] is a promising candidate with such a structure. This compound became worthy of research and study [13–15] due to its superior visible-light absorption, high chemical durability, and low cost. It possesses a number of morphologies, and reports on its properties were done either in 1D [16], 2D [17], and 3D [18] structures. To diminish the recombination of external electrons and holes on the surface of this semiconductor; many strategies can be followed. One can do it by metal composition like metal/ZnIn2S4 [19–23]. The separation of electron–hole pairs can also be done by doping the compound with the Cu, Fe, Co, and Mo cations [24–26]. Or alternatively, by introducing vacancies [27,28]. However, it is also possible to tune

[a] e-mail: ben.rerbal@gmail.com
[b] e-mail: tarik_ouahrani@yahoo.fr (corresponding author)

their electronic and optical properties as well as the photoresponse one by applying pressure [29,30].

As a new layered AM_2X_4 material, $MgIn_2Se_4$ constitutes a candidate to rejoin $ZnIn_2S_4$ like a photocatalyst semiconductor. Remarkably, this compound has the same structure as $ZnIn_2S_4$. Both structures belong to the same $R\bar{3}m$ phase, according to experimental evidence, see [31] and [32–34]. They have almost the same rigidity and nearly the same bandgap value. This phase is packed along the [001] direction and has an antisite void [32]. This fact can permit us to modulate the structure. The application of hydrostatic pressure on $MgIn_2Se_4$ leads to a phase transition to a more packed structure of nearly 2 GPa [35]. This study also indicates that hydrostatic pressure changes the nature of the bonding as well as the electronic properties, while the application of pressure up to 4 GPa can also increase the bandgap value by 3%. Schmid et al. [36] used the chemical vapor transport technique to measure the photoacoustic spectra of $MgIn_2Se_4$ single crystal at different temperatures. They showed that the bandgap value of layered $MgIn_2Se_4$ from 1.4 to 1.65 eV by increasing the temperatures from 80 to 300 K. The photoactivity of this material as regards light is very active under such conditions.

Experiments as well as theoretical studies reported that most photocatalyst bulk materials have a wide bandgap, see TiO_2 [37], $SrTiO_3$ [38], CuO [39], CdS [40], and ZnO [41]. Because of this specificity, the absorption of light is low in the visible (Vis) region. They absorb UV light, which makes them not so efficient. The cause is that even if ultraviolet (UV)–Vis solar energy reaches the earth by about 43%, only 5% is harvested on the surface. Thus, it is crucial to search for new high-competence materials or develop new methods which help harvest more solar power. This task could be done by affecting the bonding pattern of the material. One powerful method is to apply a constraint in one direction of the material. Consequently, in this way, to tune the properties of $MgIn_2Se_4$ layered compound, we have applied a uniaxial strain along the z-axis. Here, the present study will provide unbiased information on how the $MgIn_2Se_4$ layered compound will behave under such strain. We will show that due to the very ductile behavior of this material, the electronic and then the photocatalysis properties will change rapidly into only 2.5% of uniaxial strain. To do this task, a toolkit of strategy will be used, namely density functional theory (DFT) [42,43] calculations including the analysis of mechanical and dynamical stability. We will also use the topology of charge density [44] to analyze the bonding properties in the range of applied constraints.

2 Computational details

We performed DFT calculations with the Vienna Ab-initio Simulation Package (VASP) code [45,46]. To consider both the valence and the semi-core states, we have chosen the projector-augmented wave scheme (PAW) [47] implemented in this code. We also resorted to the use of semi-local functional, Perdew–Burke–Ernzerhof revised for solids (GGA-PBEsol) [48] exchange potential. This setup has been successfully used for the prediction of structural properties [30]. To achieve reliable accuracy calculations, the `PREC` tag, and other cutoff energies were chosen adequately. For example, the `ENCUT` designing the plane-wave cutoff for the basis functions was set at 470 eV; and `EDIFF` (the convergence criterion for stopping electronic relaxation) to `1E-7`. All the structures were allowed to relax according to the Hellman–Feynman forces using the conjugate gradient algorithm until all the forces acting on the atoms were less than `EDIFFG` $= -0.003$ (in eV/Å). The integration over the first Brillouin zone was made using an $8 \times 8 \times 4$ Γ-centered k-points grid generated according to the Monkhorst–Pack scheme [49]. Since the title compound has a closed shell, non-spin polarization calculations were performed. In addition, Van der Waals (vdW) corrections to the total energy were taken into account within DFT by including the dispersion interactions using the D3 method [50,51]. The calculations of bandgap value were done within the Heyd–Scuseria–Ernzerhof (HSE06) [52] hybrid functional. To check the dynamical stability and obtain the vibration characteristics, we employ the density functional perturbation theory (DFPT) as cited in [53,54], and implemented in the phonopy software [53].

3 Results and discussion

3.1 Structural properties and stability

To begin with this investigation, we should keep in mind that the structure has a rhombohedral phase in the range of pressure between 0 and 2 GPa (see the result found in Ref [35]). Therefore, structural optimization was carried out for zero pressure and zero temperature (zero-point vibrational contributions were neglected.). The relaxation of the structure gives a lattice parameter value very close to what was previously achieved in our published work [35]. Due to the use of PBEsol functional, the result is very consistent with the values found in experimental evidence of Gastaldi et al. [32]. The lattice parameters, as well as the bulk modulus (B_0) are gathered in Table 1. The result shows that, due to the small value of B_0, the title compound is very sensible to the application of hydrostatic pressure.

As a prelude to our discussion of mechanical stability, we have calculated the elastic constant of this structure. This one has six (C_{ij}) components. The calculated elastic constants are presented in Table 1. For rhombohedral system point group $\bar{3}m$, the stability criteria should satisfy the equations [55,56]:

$$(C_{11} > |C_{12}|; C_{44} > 0;$$
$$C_{13}^2 < \frac{1}{2} C_{33}(C_{11} + C_{12});$$

Table 1 Calculated lattice parameters in (Å), bulk modulus B_0 in (GPa) and elastic constants in (GPa)

	a	c	B_0	C_{11}	C_{12}	C_{13}	C_{33}	C_{44}	C_{14}	C_{66}
Calculated	4.033	39.05	35.51	48.32	25.52	25.06	72.51	10.04	6.48	11.4
Experiment [32]	4.03	39.70	–	–	–	–	–	–	–	–

Here $C_{66} = (C_{11} - C_{12})/2$

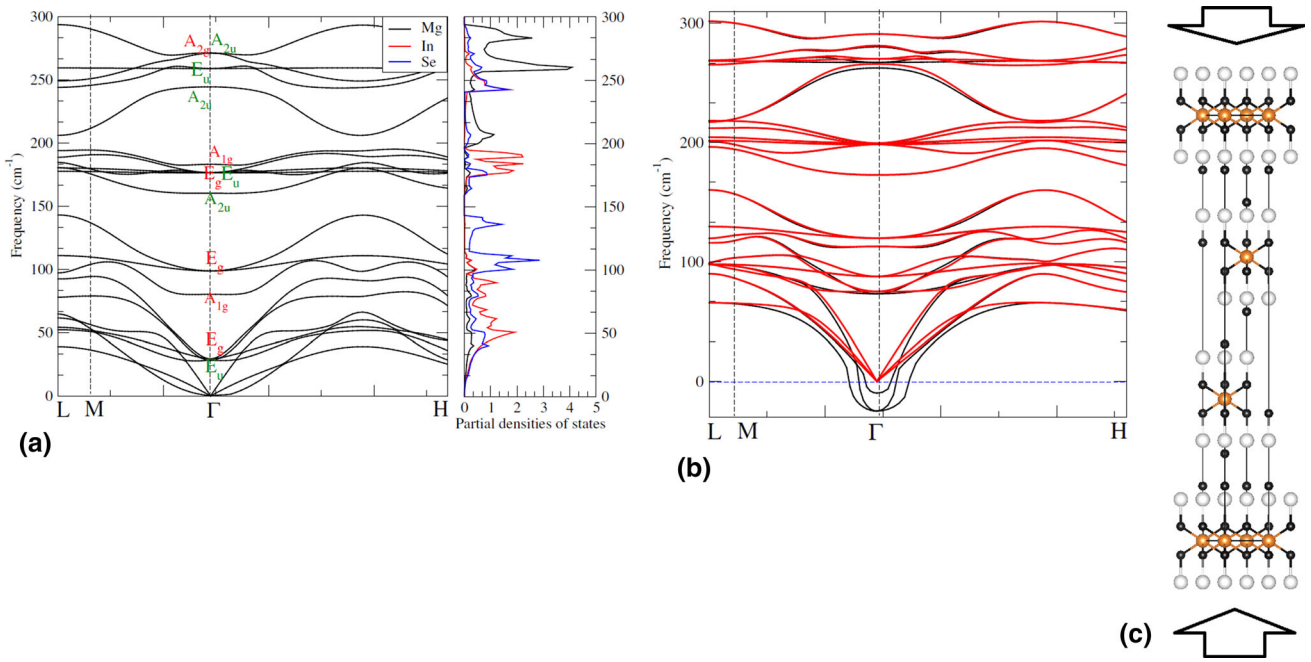

Fig. 1 The phonon dispersion curve of **a** unstrained structure and **b** under a compression strain equal to −3% in black and −2.5% in red lines, **c** gives an overview of the applied uniaxial strains on the structure

$$C_{14}^2 + C_{15}^2 < \frac{1}{2} C_{44}(C_{11} - C_{12}) = C_{44}C_{66}; \qquad (1)$$

It is to be noticed that the mechanical stability conditions involving the elastic constants in the investigated structure are seen to be satisfied.

Interesting information can be seen in Table 1: the fact that $C_{66} \simeq C_{44}$ indicates that the [100] (010) shear is almost similar to the [010] (001) shear. However, $C_{33} > C_{11}$, this means that the response to uniaxial strain in the z-axis is not negligible. The estimation of linear compressibility [57] is found to be equal to $\beta = 11.578$ TPa^{-1}, twice more important than in the xy directions. This result justified the choice to apply the strain along the z-axis.

Therefore, the application of uniaxial strain was made according to the relation $\varepsilon_{zz} = \frac{c-c_0}{c_0}$ (see Fig. 1c). c_0 and c are, respectively, the pristine lattice parameter and the strained one. Concerning the possible symmetry properties of the studied system, it is worth pointing out that no constraints were imposed during the structural relaxation. Accordingly, to ensure the stability of the studied structures, dynamical analysis was done on structures for $\varepsilon_{zz} = 0\%$ and strained ones for $\varepsilon_{zz} = -2.5\%$ and -3% (-3% of strain showed a total drift of 31.54 kbar). As expected, while the structures for 0% and −2.5% strain keep its $R\bar{3}m$ phase, the application of 3% of uniaxial strain deforms the structure and the material loses its rhombohedral symmetry [35]. This result can be analyzed by calculating the phonon spectra. The corresponding plots are gathered in Fig. 1a and b. We can easily show that there are no imaginary frequencies at Γ point for structures with 0% and −2.5% deformations. Only a small shift is shown for the phonon branch. At the center of the Brillouin zone (Γ point), we have 12 vibration modes following the decomposition: $\Gamma_{\text{acoustic}} = E_u + 2E_g$ and $\Gamma_{\text{optic}} = (2A_{1g} + 2E_g + 3A_{2g} + A_{2u})$. Here, the ($g$-type) and ($u$-type) are, respectively, Raman and IR active modes. Unfortunately, we were not able to find any experimental data to compare with. However, when we apply a uniaxial strain of −3%, instability appears in the phonon spectra of this system. The frequencies at the center of the Brillouin zone become negative, a consequence of the dynamical instability. Thus, to avoid any possible confusion, the application of uniaxial strain was kept in the range of 0 to −2.5%, keeping the stability of $MgIn_2Se_4$ in its $R\bar{3}m$ symmetry.

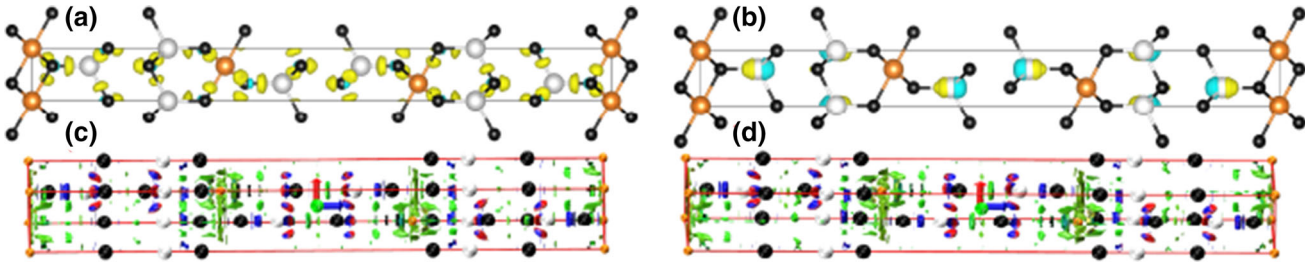

Fig. 2 In the tope, the charge density difference of **a** pristine structure for $\varepsilon_{zz} = 0\%$ and **b** strained structure for $\varepsilon_{zz} = -2.5\%$. In the bottom, NCI isosurfaces of the **c** pristine structure for $\varepsilon_{zz} = 0\%$ **d** strained structure for $\varepsilon_{zz} = -2.5\%$. Surfaces are colored in the $[-0.04, 0.04]$ a.u. range of $\text{sign}(\lambda_2)\rho(\mathbf{r})$) (isovalue $s = 0.4$ a.u.). Repulsive interactions are shown as red isosurfaces, van der Waals interactions as thin, delocalized green regions, and strong attractive interactions as localized blue lentils. The noncovalent interactions in bromine-cation bonding are circled in blue, whereas the interactions in the organic are red

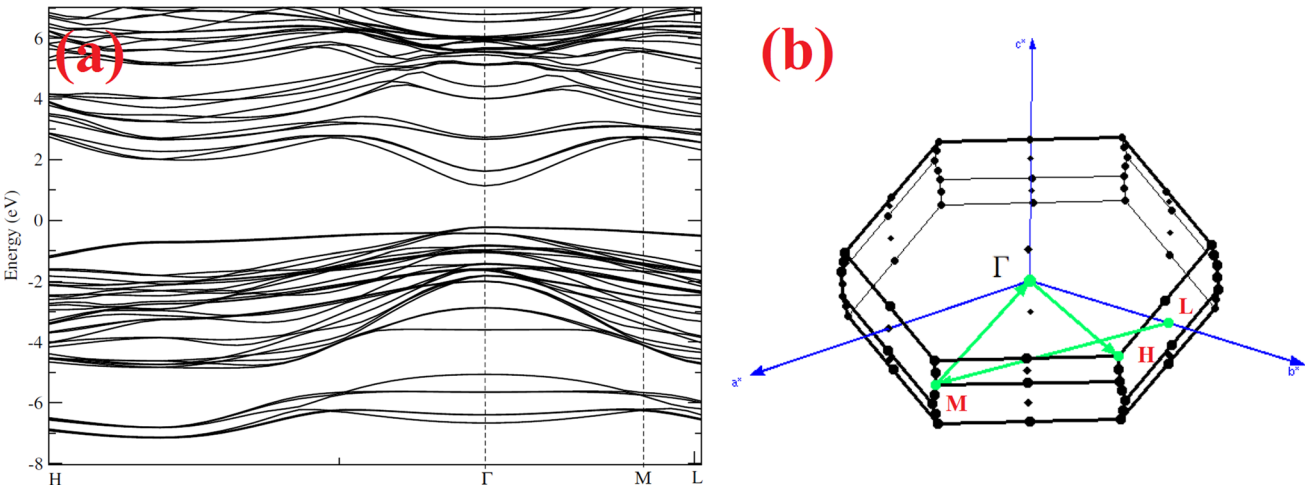

Fig. 3 **a** Band structure of the layered $MgIn_2Se_4$ compound at HSE06 level, **b** The Brillouin zone symmetry

3.2 Bonding properties

We discuss, in some detail, the bonding pattern of our structures, and analyze the consequences of the application of uniaxial strain on them. To accomplish this task, we calculated the charge difference $\Delta\rho$ between ions and cations and meticulously quantified it by extracting the Bader charges [44]. To get such charges, the electronic domains are divided into volume labeled basins (Ω) which are disjoint and additives with a space-filling zone [44,58]. In each one of these quantities, maximums and attractors are assimilated to several critical points labeled (CP). These emerge from the condition of zero flux of the gradient of the electron density: $\nabla\rho(\boldsymbol{r})\cdot\boldsymbol{n}(\boldsymbol{r}) = 0$ [44]. Figure 2a and b shows the charge difference between the unstrained and strained structures at 0 and -2.5%, respectively. It is shown that there is strong covalent bonding and a labile cloud due to an important electrostatic vdW potential. From the pristine to the strained structure, the donor and lost electron isosurfaces change dramatically. The accumulation of both isosurfaces on the In cation stipulates the enhancement of charge transfer between In and Se atoms. $Q(\text{Mg}) = +0.97\text{e}$, $Q(\text{In}) = +0.33\text{e}$, and $Q(\text{Se}) = -0.43e$ are the calculated Bader charges. The calculation of ionicity degree indicates global covalent behavior. As a consequence, the electronic properties could also be affected.

To check the noncovalent interaction change, we used the NCI index [59]. NCI can be analyzed by the identification of low ρ regions in each partitioning space [29]. However, this index shows clearly that only a weak enhancement of noncovalent interaction is happening. See the isosurface in green. The origin of such interactions corresponds to the contacts between layers. Disc-shaped surfaces in red–blue are shown between Se anions and In cations, indicating the cause of strong covalent bonding connecting these ions.

3.3 Electronic and optical properties

Up to now, we have shown that $MgIn_2Se_4$ is sensitive to strain effect if it is applied for the z-direction, as a result, the bonding properties were affected. Thus, to provide a deep insight into electronic properties under this regime, let's calculate the band structure as well as the density of states. We display in Fig. 3 the band structure of the $MgIn_2Se_4$ compound using

Table 2 Calculated bandgap, effective mass for electron (m_e^*) and hole (m_h^*) as well as the recombination ($D = m_h^*/m_e^*$).

Strain (%)	E_g (eV)	m_e^*	m_h^*	D	E_{CB}	E_{VB}
0	1.354	−2.251	0.816	0.36	−1.133	0.222
−0.5	1.409	−2.201	0.856	0.38	−1.198	0.211
−1	1.442	−2.136	0.792	0.37	−0.754	0.688
−1.5	1.457	−1.629	0.618	0.37	−1.024	0.605
−2	1.529	−2.511	0.667	0.27	−1.648	0.212
−2.5	1.879	−2.071	0.541	0.26	−1.646	0.211

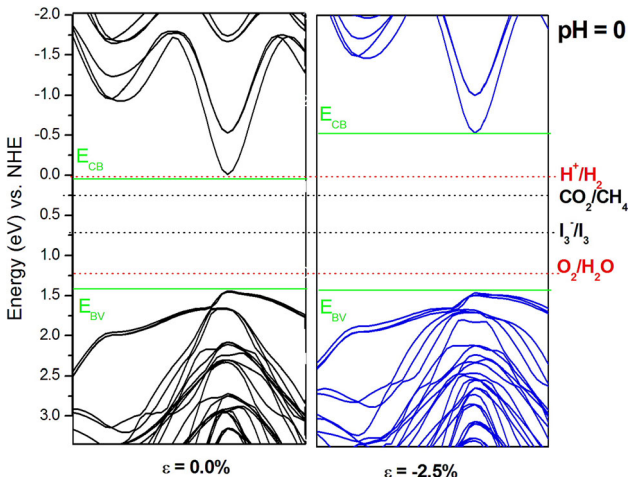

Fig. 4 Energy levels of some of the important photocatalytic reactions allowed for $\varepsilon_{zz} = 0\%$ and for $\varepsilon_{zz} = -2.5\%$ strained structures with respect to normal Hydrogen Electrode (NHE) at pH = 0. The energy levels of H^+/H_2, CO_2, and I_3/I_3^- O_2/H_2O reactions are equal, respectively, to 0.00, 0.26, 0.57, and 1.23 eV [60]

HSE06 functional along the extended Brillouin zone ($H - -\Gamma - -L - -M$). It is seen that the conduction band minimum (CBM) and valence band maximum (VBM) are found to be at Γ high symmetry point, which stipulates that $MgIn_2Se_4$ has a direct bandgap favoriting a direct transition of an excited electron from the VBM level to the CBM one.

The calculated bandgap value at the pristine structure is found to be equal to 1.354 eV, in good agreement with the measured one at 80K of 1.40 eV [36]. In addition, as the positions of the CBM and the VBM are a very crucial requirement in photocatalytic activities; their values have been calculated and gathered in Table 2.

To check the rate of recombination of e^-–h^+ pairs, we first calculated their respective effective masses by the parabolic fitting at the conduction band (CB) and valence band (VB) in the band structure obtained by the hybrid calculations. Then, we estimated the ratio of $D = m_h^*/m_e^*$ [61], m_h^* and m_e^* being, respectively, the effective mass of holes and electrons. The calculated values are gathered in Table 2. According to the results, the title compound has a value of D far from unity, which indicates a significant difference in carrier mobilities for e^- and h^+. This separation of carriers makes their recombination hard. Next, we also evaluate the reduction and oxidation potentials of CB and the VB edges at the point of zero charge by the following formula:

$$E_{CB} = \chi - E^C - (E_g/2)$$
$$E_{VB} = \chi - E_{CB} + E_g \quad (2)$$

where E_{CB} and E_{VB} are, respectively, potentials of conduction and valence band edges, E^C is the free energy corresponding to the hydrogen scale. E_g is the bandgap value, and finally χ is the electronegativity of the investigated semiconductors. It can be considered as the geometric mean of the absolute electronegativities of the constituent atoms. The results are also displayed in Table 2.

To see the effect of strain on the photocatalytic properties, both the band edge level of pristine and strained structure for $\varepsilon_{zz} = -2.5\%$ are shown in Fig. 4 (Here, the y-axis is set for Normal Hydrogen Electrode (NHE) level at pH = 0, see Eq. 2). This figure shows the reduction and oxidation levels of some of the common photocatalytic reactions with reference to vacuum and the NHE at acid solution (pH = 0) [60]. We can show in this figure the expected energy level diagram (potential vs. NHE) and CO_2, I_3/I_3^- and NO/NO_3^- photoreduction, displaying the relative positions of CB and VB levels for both strained and pristine structures. For both structures, the VB top lies above the O_2/H_2O redox potential (1.23 eV). However, only the CB level in the case of the structure for $\varepsilon_{zz} = -2.5\%$ lies above the redox potential H^+/H_2. Consequently, it appears that the pristine structure is a more efficient photocatalyst for CO_2 and I_3/I_3^- photoreduction than for photocatalysis production, and the strained semiconductor is rather devoted to producing H_2 under light irradiation. If we add the fact that the rate of D is decreasing from 0 to −2.5% of application of strain. We can conclude that the suppression of the recombination of the e^-–h^+ pairs is enhanced in this regime, leading to an increase of photocatalytic efficiency in the strained structure along the z-direction.

To obtain a rough picture of the energetic dependence of each orbital, especially the s, p and d states, we give in Fig. 5a–c, the plots of the partial density of states (PDOS). It is seen that the bottom bands are related mostly to In-d states, where these states lie

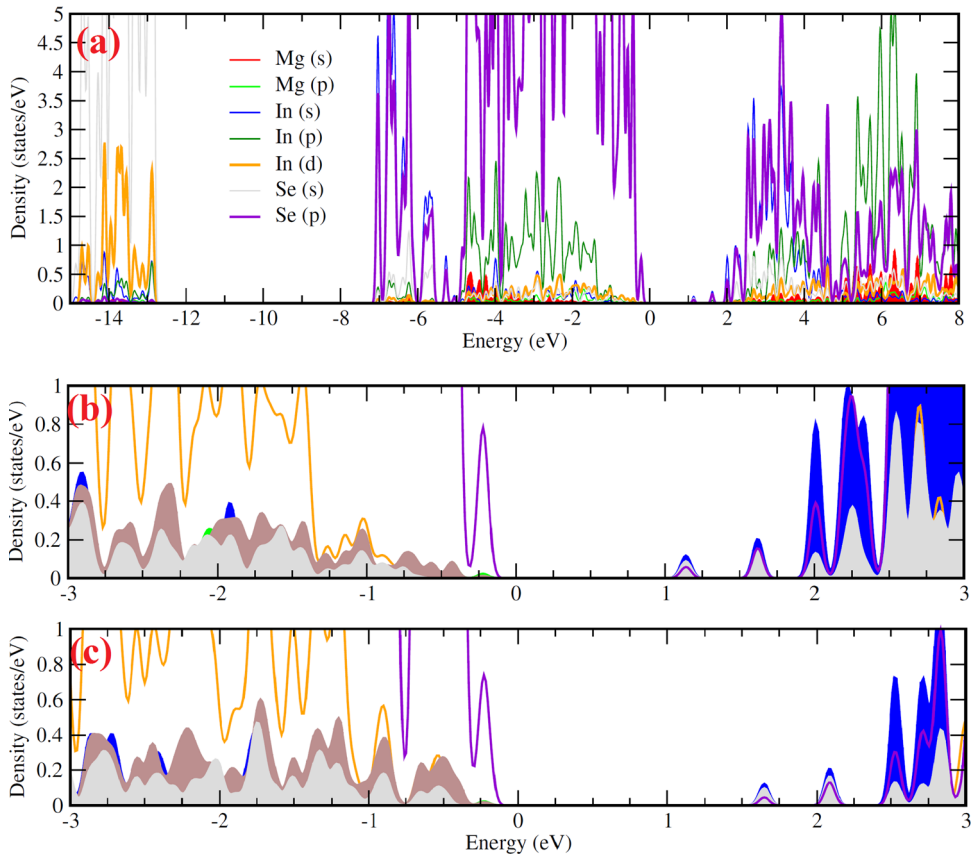

Fig. 5 **a** Partial densities of states of the layered $MgIn_2Se_4$ compound at HSE06 level, **b** and **c** give a zoom over a range of −3 to 3 eV of unstained (0%) and strained (−2.5%) structures, respectively

deeply at −15 to 13 eV. This orbital is also very pronounced near the Fermi level, while creating a strong hybridization within the Se-*p* one. The contribution of Mg-*p* also forms some peaks inside this hybridization. Finally, no lone pair is detected due to the position of Se-*s* states at −15 to −13 eV of the spectra. This analysis stipulates that the VBM–CBM energy difference (bandgap) can be seen as a measure of the energy of the charge transfer from the Se orbitals to the In orbitals, and the dominant covalent bonding is mainly due to the strong hybridization between these two ions. This explains how negative and positive charges accumulate in the In units while the structure is subjected to uniaxial strains. We have plotted in Fig. 5b and c a zoom over the electronic −3 to 3 eV range of the PDOs spectra. It is seen that the arrangement of orbitals is not very affected, However, a small increase in the In-*d* states is shown. This tends to increase the In-*d*/Se-*p* hybridization and, consequently, the covalent bonding in the strained compound.

The other crucial issue in photocatalytic activities is the size of the optical properties. Therefore, the absorption spectrum is also being investigated. To calculate this quantity, we used DFT within the Random Phase Approximation (RPA) approach in which the local field effects are included at the Hartree level only. Only inter-band transitions are taken into account, so there may be inaccuracy in dielectric function at low energies. For a translationally invariant system, the Fourier transform of the frequency-dependent symmetric dielectric matrix in the RPA is given by [62]

$$\varepsilon_{G,G'}(q,\omega) = \delta_{G,G'}(q,\omega) - \frac{4^2}{|G+q||G'+q|}\chi^0_{G,G'}(q,\omega) \tag{3}$$

where G and are reciprocal lattice vectors and q stands for the Bloch vector of the incident wave. The matrix is the irreducible polarizability matrix in the case of the independent particles derived by Adler and Wiser [63,64] in the context of the self-consistent field approach. VASP calculates the frequency-dependent dielectric matrix after the electronic ground state has been determined. The imaginary part is determined by a summation over empty states using the equation

$$\epsilon''_{\alpha\beta} = \frac{4^2}{\Omega}\lim_{q\longrightarrow 0}\frac{1}{q^2}\sum_{c,v,k} 2\omega_k\delta(\epsilon_{ck}-\epsilon_{vk}-\omega) < u_{ck+e_\alpha k}|u_{vk} >< u_{ck+e_\beta k}|u_{vk} > \tag{4}$$

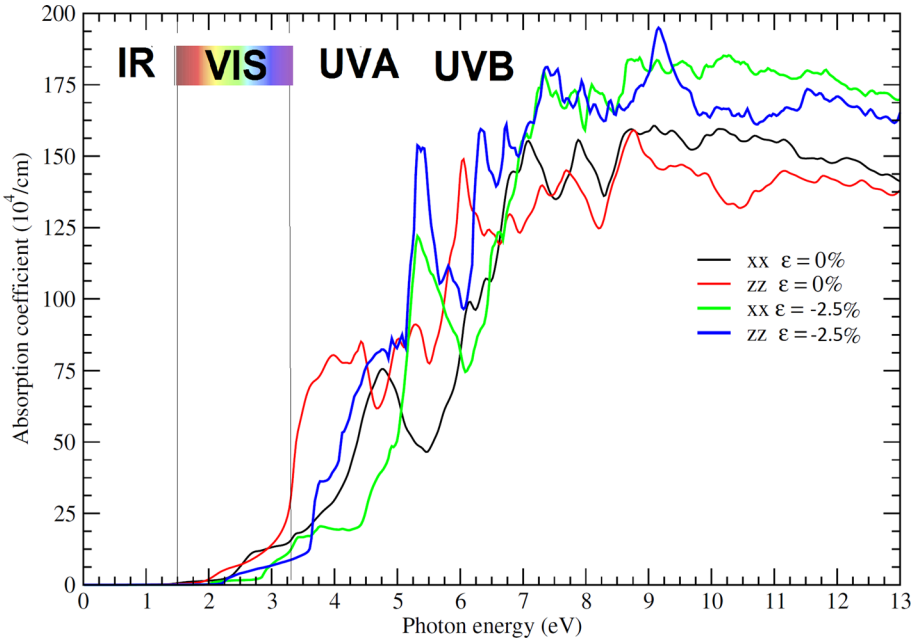

Fig. 6 The absorption spectra of strained and unstrained structure for in-plane (xx) and out-plane (zz) polarizability tensor

where the indices α and β are the Cartesian components, vectors e_α and e_β are the unit vectors along three directions, and v refer to conduction and valence band states, respectively, ϵ_{ck} refers to the energy of the conduction band and ϵ_{vk} refers to the energy of the valence band, and u_{ck} is the cell periodic part of the orbitals at the k-point **k**.

A strong (visible) light absorption with a bandgap varying between 1.8 and 2.4 eV is required for an ideal photocatalytic material [65]. For this aim, interband energetic transitions coming from the HSE06 band structure have been used to calculate the linear optical properties, and from them, the absorption spectra. The absorption spectra are calculated following the formula: $I(\omega) = \frac{2\omega}{c}\sqrt{(1/2 \times (\varepsilon_1^2(\omega) + \varepsilon_2^2(\omega))^{1/2}) - \varepsilon_1(\omega)}$. $\varepsilon(\omega)$ being the macroscopic dielectric function evaluated from permitted transitions, i.e., the interband contributions (the indexing by 1 and 2, respectively, indicate the real and imaginary parts of the dielectric function) and c is the speed of light in a vacuum. The frequency-dependent absorption coefficient spectra are displayed in Fig. 6. From this figure, we can show that $MgIn_2Se_4$ compound depicts the spectral limits of a semiconductor type wherein the edge of the Vis–UV region is reached by absorption of resonant frequency photons. Both pristine and strained structures have a significant contribution that lies in the energy of solar radiation (in the interval from 1.4 to 3.2 eV). The curve shows a particular energy range in the middle and deep UV regions with small oscillations at higher energies. The maximum main absorption peak barycentre is localized in the UV. However, the first absorption valley is rather situated in the deep UV range, where its most important peaks depend upon the quantitative contribution of transitions from In-d to Se-p orbitals. The arrangement of peaks is relatively in concordance with the permitted interband transitions. By increasing the compressive strains, we show, nevertheless, a shift in the optical bandgap while the strain is increased. Thus, the strained compound begins to be more suitable for redox potential H^+/H_2 reaction. This property is already shown in the plot of NHE level at pH = 0. This makes the title compound, whether in its equilibrium structure or strained one, a good choice for the photocatalytic disinfection process or for photocatalytic producing green energy. The application of strain seems a useful solution to allow absorption of light in a larger game going from the visible to the far UV spectrum.

4 Conclusion

The analysis of the mechanical properties of the layered $MgIn_2Se_4$ compound allowed us to propose modulation of its properties along the z-direction. This task was done by means of ab initio calculations within the DFT strategy. As the first step in our study, the equilibrium structure has been calculated and found to be in good agreement with experimental evidence. The elastic constants were calculated for the first time for this compound. Their analysis shows that the investigated material is rather anisotropic and its z-direction is very sensitive to directional pressure. To achieve this aim, we have applied an external strain in this direction. We found that the investigated compound stays stable up to compression of −2.5%. After this percentage, a dynamical instability was predicted. All vibra-

tional modes (Raman and infrared) have been assigned and related to atomic vibrations. The application of external pressure provided a unique way to investigate the relationship between structural and electronic properties. The use of HSE06 permits getting a bandgap value in good agreement with the measured one. Many properties, including effective mass and recombination rate, were calculated using this approach. Then, these properties were also analyzed under the effect of uniaxial strain. This one allowed us to build an energy level diagram as a function of photocatalytic activities. Overall, we found that the strained structure with a −2.5% of distortion is very promising for photocatalyst green reaction, whereas the pristine structure is rather devoted to reduction and disinfection of pollutants. Finally, the adsorption coefficient was also calculated. The result shows that $MgIn_2Se_4$ can absorb light in a large range of Vis–UV as well as in the UV spectrum.

Author contributions

TO conceived and designed the project. BR performed the calculations. All the authors analyzed and discussed the results.

Data availability All relevant data are available from the corresponding author upon reasonable request.

Declarations

Conflict of interest The authors declare that they have no known competing financial interests or personal relationships that could have appeared to influence the work reported in this paper.

Credit authorship contribution statement
Benali Rerbal: investigation and original draft.
Tarik Ouahrani: conceptualization and formal analysis, writing—review and editing, resources, supervision.

Author information Readers are welcome to comment on the online version of the paper. Correspondence and requests for materials should be addressed to T.O. (tarik_ouahrani@yahoo.fr) or B.R. (ben.rerbal@gmail.com).

References

1. P. Kulkarni, S. Chellam, Disinfection by-product formation following chlorination of drinking water: artificial neural network models and changes in speciation with treatment. Sci. Total Environ. **408**, 4202–4210 (2010). https://doi.org/10.1016/j.scitotenv.2010.05.040
2. B. Song, X. Sun, Y. Jiang, Y. Li, L.U. Che, Formation of disinfection by-products during chlorine dioxide pre-oxidation of chironomid larvae metabolites followed by chlorination. Desalin. Water Treat. **57**, 28698–28704 (2016). https://doi.org/10.1080/19443994.2016.1195286
3. S. Nishizawa, T. Matsushita, Y. Matsui, N. Shirasaki, Formation of disinfection byproducts from coexisting organic matter during vacuum ultraviolet (VUV) or ultraviolet (UV) treatment following pre-chlorination and their fates after postchlorination. Sci. Total Environ. **737**, 140300 (2020). https://doi.org/10.1016/j.scitotenv.2020.140300
4. W.J. Wang, G.C. Huang, J.C. Yu, P.K. Wong, Advances in photocatalytic disinfection of bacteria: development of photocatalysts and mechanisms. J. Environ. Sci. **34**, 232–247 (2015). https://doi.org/10.1016/j.jes.2015.05.003
5. Z. Xiong, L. Huang, J. Peng, Y. Hou, Z. Ding, S. Wang, Spinel-type mixed metal sulfide $NiCo_2S_4$ for efficient photocatalytic reduction of CO_2 with visible light. ChemCatChem. **11**, 5513–5518 (2019). https://doi.org/10.1002/cctc.201901379
6. S. Chang, Y. Hu, J. Qian, Y. Shao, S. Ni, L. Kong, W. Dan, C. Luo, S. Jin, X. Xu, Mg_2TiO_4 spinel modified by nitrogen doping as a visible-light-active photocatalyst for antibacterial activity. Chem. Eng. J. **410**, 128410 (2021). https://doi.org/10.1016/j.cej.2021.128410
7. S. Wang, Z. Ding, X. Wang, A stable $ZnCo_2O_4$ cocatalyst for photocatalytic CO2 reduction. Chem. Commun. **51**, 1517 (2015). https://doi.org/10.1039/C4CC07225A
8. Z. Wang, M. Jiang, J. Qin, H. Zhou, Z. Ding, Reinforced photocatalytic reduction of CO2 to CO by a ternary metal oxide NiCo2O4. Phys. Chem. Chem. Phys. **17**, 16040 (2015). https://doi.org/10.1039/C5CP01997D
9. S. Wang, B.Y. Guan, X.W. Lou, Rationally designed hierarchical N-doped carbon@$NiCo_2O_4$ double-shelled nanoboxes for enhanced visible light CO_2 reduction. Energy Environ. Sci. **11**, 306 (2018). https://doi.org/10.1039/C7EE02934A
10. M. Jiang, Y. Gao, Z. Wang, Z. Ding, Photocatalytic CO2 reduction promoted by a $CuCo_2O_4$ cocatalyst with homogeneous and heterogeneous light harvesters. Appl. Catal. B **198**, 180 (2016). https://doi.org/10.1016/j.apcatb.2016.05.055
11. S. Wang, Y. Hou, X. Wang, Development of a stable $MnCo_2O_4$ cocatalyst for photocatalytic CO_2 reduction with visible light. ACS Appl. Mater. Interf. **7**, 4327 (2015). https://doi.org/10.1021/am508766s
12. G. Zhang, H. Wu, D. Chen, N. Li, Q. Xu, H. Li, J. He, J. Lu, A mini-review on $ZnIn_2S_4$-Based photocatalysts for energy and environmental application. Green Energy Environ. (2021). https://doi.org/10.1016/j.gee.2020.12.015
13. Y. Chen, R. Huang, D. Chen, Y. Wang, W. Liu, X. Li, Z. Li, Exploring the different photocatalytic performance for dye degradations over hexagonal $ZnIn_2S_4$ microspheres and cubic $ZnIn_2S_4$ nanoparticles. ACS Appl. Mater. Interfaces **4**, 2273–2279 (2012). https://doi.org/10.1021/am300272f
14. J. Wang, Y. Chen, W. Zhou, G. Tian, Y. Xiao, H. Fu, H. Fu, Cubic quantum dot/hexagonal microsphere $ZnIn_2S_4$ heterophase junctions for exceptional visible-light-driven photocatalytic H2 evolution. J. Mater. Chem. A **5**, 8451–8460 (2017). https://doi.org/10.1039/C7TA01914A
15. Y. Chen, S. Hu, W. Liu, X. Chen, L. Wu, X. Wang, P. Liu, Z. Li, Controlled syntheses of cubic and hexagonal $ZnIn_2S_2$ nanostructures with different visible-light pho-

tocatalytic performance. Dalton Trans. **40**, 2607–2613 (2011). https://doi.org/10.1039/C0DT01435D
16. X. Feng, K. Shankar, O.K. Varghese, M. Paulose, T.J. Latempa, C.A. Grime, Vertically aligned single crystal TiO_2 nanowire arrays grown directly on transparent conducting oxide coated glass: synthesis details and applications. Nano Lett. **8**, 3781–3786 (2008). https://doi.org/10.1021/nl802096a
17. M.-Q. Yang, Y.-J. Xu, W. Lu, K. Zeng, H. Zhu, Q.-H. Xu, G.W. Ho, Self-surface charge exfoliation and electrostatically coordinated 2D hetero-layered hybrids. Nat. Commun. **8**, 14224 (2017). https://doi.org/10.1038/ncomms14224
18. N.S. Chaudhari, S.S. Warule, B.B. Kale, Architecture of rose and hollow marigold-like $ZnIn_2S_4$ flowers: structural, optical and photocatalytic study. RSC Adv. **4**, 12182–12187 (2014). https://doi.org/10.1039/C3RA45767B
19. Y. Li, K. Zhang, S. Peng, G. Lu, S. Li, Photocatalytic hydrogen generation in the presence of ethanolamines over $Pt/ZnIn_2S_4$ under visible light irradiation. J. Mol. Catal. A Chem. **363**, 354–361 (2012). https://doi.org/10.1016/j.molcata.2012.07.011
20. B. Wang, Z. Deng, X. Fu, C. Xu, Z. Li, Photodeposition of Pd nanoparticles on $ZnIn_2S_4$ for efficient alkylation of amines and ketones' α-H with alcohols under visible light. Appl. Catal. B Environ. **237**, 970–975 (2018). https://doi.org/10.1016/j.apcatb.2018.06.067
21. T. Zhu, X. Ye, Q. Zhang, Z. Hui, X. Wang, S. Chen, Efficient utilization of photogenerated electrons and holes for photocatalytic redox reactions using visible light-driven $Au/ZnIn_2S_4$ hybrid. J. Hazard Mater. **367**, 277–285 (2019). https://doi.org/10.1016/j.jhazmat.2018.12.093
22. C. Feng, X. Yang, Z. Sun, J. Xue, L. Sun, J. Wang, Z. He, J. Yu, Dual interfacial synergism in $Au\text{-}Pd/ZnIn_2S_4$ for promoting photocatalytic selective oxidation of aromatic alcohol. Appl. Surf. Sci. **501**, 144018 (2020). https://doi.org/10.1016/j.apsusc.2019.144018
23. H. An, M. Li, R. Liu, Z. Gao, Z. Yin, Design of AgxAu1-x alloy/$ZnIn_2S_4$ system with tunable spectral response and Schottky barrier height for visible-light-driven hydrogen evolution. Chem. Eng. J. **382**, 122953 (2020). https://doi.org/10.1016/j.cej.2019.122953
24. S. Shen, L. Zhao, Z. Zhou, L. Guo, Enhanced photocatalytic hydrogen evolution over Cu-doped $ZnIn_2S_4$ under visible light irradiation. J. Phys. Chem. C **112**, 16148–16155 (2008). https://doi.org/10.1021/jp804525q
25. W.-H. Yuan, X.-C. Liu, L. Li, Improving photocatalytic performance for hydrogen generation over Co-doped $ZnIn_2S_4$ under visible light. Acta Phys. Chim. Sin. **29**, 151–156 (2013). https://doi.org/10.3866/PKU.WHXB201210093
26. B. Gao, L. Liu, J. Liu, F. Yang, Photocatalytic degradation of 2,4,6-tribromophenol over Fe-doped $ZnIn_2S_4$: stable activity and enhanced debromination. Appl. Catal. B Environ. **129**, 89–97 (2013). https://doi.org/10.1016/j.apcatb.2012.09.007
27. H.-X. Fang, H. Guo, C.-G. Niu, C. Liang, D.-W. Huang, N. Tang, H.-Y. Liu, Y.-Y. Yang, L. Li, Hollow tubular graphitic carbon nitride catalyst with adjustable nitrogen vacancy: enhanced optical absorption and carrier separation for improving photocatalytic activity. Chem. Eng. J. **402**, 126185 (2020). https://doi.org/10.1016/j.cej.2020.126185
28. H. Yu, J. Huang, L. Jiang, Y. Shi, K. Yi, W. Zhang, J. Zhang, H. Chen, X. Yuan, Enhanced photocatalytic tetracycline degradation using N-CQDs/OV-BiOBr composites: unraveling the complementary effects between N-CQDs and oxygen vacancy. Chem. Eng. J. **402**, 126187 (2020). https://doi.org/10.1016/j.cej.2020.126187
29. H.Z. Guedda, T. Ouahrani, A. Morales-García, R. Franco, M.A. Salvado, P. Pertierra, J.M. Recio, Computer simulations of 3C-SiC under hydrostatic and non-hydrostatic stresses. Phys. Chem. Chem. Phys. **18**, 8132–8139 (2016). https://doi.org/10.1039/C6CP00081A
30. T. Ouahrani, F.-Z. Medjdoub, S. Gueddida, Á. Lobato Fernandez, R. Franco, N.-E. Benkhettou, M. Badawi, A. Liang, J. Gonzalez, D. Errandonea, Understanding the pressure effect on the elastic, electronic, vibrational, and bonding properties of the CeScO3 perovskite. J. Phys. Chem. C **125**(1), 107–119 (2021). https://doi.org/10.1021/acs.jpcc.0c08641
31. S.A. Lopez-Rivera, A.J. Mora, D.A. Najarro, A.V. Rivera, R.A. Godoy, Determination of the structure of IIIa-$ZnIn_2S_4$ using convergent-beam electron diffraction and single-crystal x-ray diffraction. Semicond. Sci. Technol. **16**, 367–371 (2001). https://doi.org/10.1088/0268-1242/16/5/315
32. L. Gastaldi, A. Maltese, S. Viticoli, Crystal growth of the layered $MgIn_2Se_4$ compound. J. Cryst. Growth **66**, 673–675 (1984). https://doi.org/10.1016/0022-0248(84)90167-2
33. P. Dotzel, H. Schafer, G. Schon, Anorg. Allg. Chem. **426**, 260 (1976)
34. J. Chem, K.-J. Range, Z. Naturforsch, B Sci. **51**, 1363–1364 (1996)
35. K. Boukri, T. Ouahrani, M. Badawi, K. Demmouche, R. Franco, J.M. Recio, "Disclosing the behavior under hydrostatic pressure of rhombohedral $MgIn_2Se_4$ by means of first-principles calculations. Phys. Chem. **22**, 21909–21918 (2020). https://doi.org/10.1039/D0CP02842H
36. R. Schmid, K. Friemelt, E. Bucher, Optical and electrical properties of the ternary, layer-structured compound $MgIn_2Se_4$. Phys. Stat. Sol. **161**, 549 (1997). https://doi.org/10.1002/1521-396X(199706)161:2⟨549::AID-PSSA549⟩3.0.CO;2-5
37. M.N. Islam, J. Podder, The role of Al and Co co-doping on the band gap tuning of TiO2 thin films for applications in photovoltaic and optoelectronic devices. Mater. Sci. Semicond. Process. **121**, 105419 (2021). https://doi.org/10.1016/j.mssp.2020.105419
38. M. Kumar, P. Basera, S. Saini, S. Bhattacharya, Role of defects in photocatalytic water splitting: monodoped vs codoped $SrTiO_3$. J. Phys. Chem. C **124**, 10272–10279 (2020). https://doi.org/10.1021/acs.jpcc.9b11160
39. R. Katal, S. Masudy-panah, E.Y.J. Kong, N. Dasineh Khiavi, M.H.D. Abadi Farahani, X. Gong, Nanocrystal-engineered thin CuO film photocatalyst for visible-lightdriven photocatalytic degradation of organic pollutant in aqueous solution. Catal. Today **340**, 236–244 (2020). https://doi.org/10.1016/j.cattod.2018.12.019

40. Z. Yu, L. Qian, T. Zhong, Q. Ran, J. Huang, Y. Hou, F. Li, M. Li, Q. Sun, H. Zhang, Enhanced visible light photocatalytic activity of CdS through controllable self-assembly compositing with ZIF-67. Mol. Catal. **485**, 110797 (2020). https://doi.org/10.1016/j.mcat.2020.110797
41. I. Ahmad, S. Shukrullah, M. Ahmad, E. Ahmed, M.Y. Naz, M.S. Akhtar, N.R. Khalid, A. Hussain, I. Hussain, Effect of Al doping on the photocatalytic activity of ZnO nanoparticles decorated on CNTs and graphene: solvothermal synthesis and study of experimental parameters. Mater. Sci. Semicond. Process. **123**, 105584 (2021). https://doi.org/10.1016/j.mssp.2020.105584
42. P. Hohenberg, W. Kohn, Inhomogeneous electron gas. Phys. Rev. B **864**, 136 (1964). https://doi.org/10.1103/PhysRev.136.B864
43. W. Kohn, L.J. Sham, Quantum density oscillations in an inhomogeneous electron gas. Phys. Rev. **137**, A1697 (1965). https://doi.org/10.1103/physrev.137.a1697
44. R.F.W. Bader, *Atoms in Molecules: A Quantum Theory* (Clarendon Press, Oxford, 1990), p. 438
45. G. Kresse, J. Hafner, Ab initio molecular dynamics for liquid metals. Phys. Rev. B **47**, 558–561 (1993). https://doi.org/10.1103/PhysRevB.47.558
46. G. Kresse, J. Furthmüller, Efficiency of ab-initio total energy calculations for metals and semiconductors using a plane-wave basis set. Comput. Mat. Sci. **6**, 15–50 (1996). https://doi.org/10.1016/0927-0256(96)00008-0
47. P.E. Bloch, Projector augmented-wave method. Phys. Rev. B **50**, 17953–17979 (1994). https://doi.org/10.1103/PhysRevB.50.17953
48. J.P. Perdew, A. Ruzsinszky, G.I. Csonka, O.A. Vydrov, G.E. Scuseria, L.A. Constantin, X. Zhou, K. Burke, Restoring the density-gradient expansion for exchange in solids and surfaces. Phys. Rev. Lett. **100**, 136406 (2008). https://doi.org/10.1103/PhysRevLett.100.136406
49. H.J. Monkhorst, J.D. Pack, Special points for Brillouin-zone integrations. Phys. Rev. B **13**, 5188–5192 (1976). https://doi.org/10.1103/physrevb.13.5188
50. S. Grimme, J. Antony, S. Ehrlich, S. Krieg, A consistent and accurate ab initio parametrization of density functional dispersion correction (DFT-D) for the 94 elements H-Pu. J. Chem. Phys. **132**, 154104 (2010). https://doi.org/10.1063/1.3382344
51. S. Grimme, S. Ehrlich, L. Goerigk, Effect of the damping function in dispersion corrected density functional theory. J. Comp. Chem. **32**, 1456 (2011). https://doi.org/10.1002/jcc.21759
52. J. Heyd, G.E. Scuseria, M. Ernzerhof, Hybrid functionals based on a screened Coulomb potential. J. Chem. Phys. **118**, 8207 (2003). https://doi.org/10.1063/1.1564060
53. A. Togo, F. Oba, I. Tanaka, First-principles calculations of the ferroelastic transition between rutile-type and $CaCl_2$-type SiO_2 at high pressures. Phys. Rev. B **78**, 134106 (2008). https://doi.org/10.1103/PhysRevB.78.134106
54. S. Baroni, S. de Gironcoli, A. Dal Corso, P. Gianozzi, Phonons and related crystal properties from density-functional perturbation theory. Rev. Mod. Phys. **73**, 515 (2001). https://doi.org/10.1103/RevModPhys.73.515
55. M. Born, H. Huang, *Dynamical Theory of Crystal Lattices* (Clarendon, Oxford, 1954)
56. F. Mouhat, F.-X. Coudert, Necessary and sufficient elastic stability conditions in various crystal systems. Phys. Rev. B **90**, 224104 (2014). https://doi.org/10.1103/PhysRevB.90.224104
57. T. Ouahrani, Y.Ö. Çiftci, M. Mebrouki, Dynamical and anisotropic behavior of the $MSiP_2$ (M= Be, Mg, Cd, Zn and Hg) compounds. J. Alloys. Compd. **610**, 372–381 (2014). https://doi.org/10.1016/j.jallcom.2014.04.172
58. T. Ouahrani, I. Merad-Boudia, H. Baltache, R. Khenata, Z. Bentalha, Effect of pressure on the global and local properties of cubic perovskite crystals. Phys. Scr. **84**, 025704 (2011). https://doi.org/10.1088/0031-8949/84/02/025704
59. E.R. Johnson, S. Keinan, P. Mori-Sanchez, J. Contreras-Garcia, A.J. Cohen, W. Yang, Revealing noncovalent interactions. J. Am. Chem. Soc. **132**, 6498–6506 (2010). https://doi.org/10.1021/ja100936w
60. W.N. Wang, J. Soulis, Y. Jeffrey Yang, P. Biswas, Comparison of CO_2 photoreduction systems: a review. Aerosol Air Qual. Res. **14**, 533–549 (2014). https://doi.org/10.4209/aaqr.2013.09.0283
61. H.J. Zhang, L. Liu, Z. Zhou, Towards better photocatalysts: first-principles studies of the alloying effects on the photocatalytic activities of bismuth oxyhalides under visible light. Phys. Chem. Chem. Phys. **14**, 1286–1292 (2012). https://doi.org/10.1039/C1CP23516H
62. M. Gajdoš, K. Hummer, G. Kresse, Linear optical properties in the projector-augmented wave methodology. Phys. Rev. B **73**, 045112 (2006). https://doi.org/10.1103/PhysRevB.73.045112
63. S.L. Adler, Quantum theory of the dielectric constant in real solids. Phys. Rev. **126**, 413 (1962). https://doi.org/10.1103/PhysRev.126.413
64. N. Wiser, Dielectric constant with local field effects included. Phys. Rev. **129**, 62 (1963). https://doi.org/10.1103/PhysRev.126.413
65. K. Maeda, K. Teramura, D. Lu, T. Takata, N. Saito, Y. Inoue, K. Domen, Photocatalyst releasing hydrogen from water. Nature **440**, 295 (2006). https://doi.org/10.1038/440295a